Supplementary file

Efficient optimization of coupled geothermal reservoir modeling and power plant off-design based on deep learning

Ziyou Liu, Manojkumar Gudala, Bicheng Yan*

Physical Science and Engineering (PSE) Division, King Abdullah University of Science and Technology (KAUST), Thuwal 23955-6900, Saudi Arabia

E-mail address: ziyou.liu@kaust.edu.sa (Z. Liu); manojkumar.gudala@kaust.edu.sa (M. Gudala); bicheng.yan@kaust.edu.sa (B. Yan).

* Corresponding author. ORCID: 0000-0002-3356-7594 (B. Yan)

Liu, Z., Gudala, M., Yan, B. Efficient optimization of coupled geothermal reservoir modeling and power plant off-design based on deep learning. Advances in Geo-Energy Research, 2025, 18(1): 84-98.

The link to this file is: https://doi.org/10.46690/ager.2025.10.07

Appendix A: Supplementary equations

The geothermal energy recovery process from hot sedimentary aquifer (HSA) involves heat transfer, fluid flow, and mechanical deformation, which can be described by a thermo–hydro–mechanical (THM) coupling model (Aliyu and Chen, 2017; Cao et al., 2022). The energy conservation equation in rock matrix considering heat conduction and convection is given as:

$$\rho_m C_{p,m} \nabla_t T + \rho_w C_{p,w} v \cdot \nabla T - \nabla(\lambda_m \cdot \nabla T) = 0 \quad (1)$$

where ρ is density, C_p is the specific heat capacity, T is the temperature, t is time, v is the Darcy velocity given by Darcy's law, and λ is the thermal conductivity. The subscripts m and w represent properties of the matrix and water, respectively. The properties of the matrix can be expressed using the mixing rule:

$$\rho_m = \phi\rho_w + (1-\phi)\rho_s \quad (2)$$
$$C_{p,m} = \phi C_{p,w} + (1-\phi)C_{p,s} \quad (3)$$
$$\lambda_m = \phi\lambda_w + (1-\phi)\lambda_s \quad (4)$$

where ϕ is porosity. The subscript s represents the solid state and w indicates the liquid state.

Darcy's law is expressed as:

$$v = -\frac{k}{\mu_w}(\nabla p - \rho_w g) \quad (5)$$

where k is permeability, μ is viscosity, p is pressure, and g is gravity.

The governing equation of fluid flow in a porous reservoir is expressed as:

$$\frac{\partial(\phi\rho_w)}{\partial t} + \nabla \cdot (\rho_w v) = -\rho_w \alpha_b \frac{\partial \varepsilon_{vol}}{\partial t} \quad (6)$$

where α_b is the Biot–Willis coefficient and ε_{vol} is the volumetric strain. The term on the right-hand side is the coupling term of fluid flow and geomechanics. The Biot–Willis coefficient can be calculated by:

$$\alpha_b = 1 - \frac{K_d}{K_{fl}} \quad (7)$$

where K_d and K_{fl} are drained bulk modules and fluid bulk modules, respectively.

The poroelastic storage process can be expressed as:

$$\frac{\partial(\phi\rho_w)}{\partial t} = \frac{\rho_w}{M}\frac{\partial p}{\partial t} \quad (8)$$

where M is Biot's modulus defined as follows (Biot, 1955):

$$\frac{1}{M} = \frac{\phi}{K_{fl}} + (\alpha_b - \phi)\frac{1-\phi}{K_d} \quad (9)$$

In addition to the reservoir model, a nonisothermal wellbore model was developed to account for heat loss in the production wellbore. The energy balance equation is expressed as:

$$\rho_w A C_{p,w} u \boldsymbol{e}_t \cdot \nabla_t T = \nabla_t \cdot (A \lambda_w \nabla_t T) + \frac{1}{2} f_D \frac{\rho_w A}{d_h} |u| u^2 + Q + Q_b \tag{10}$$

where A is the wellbore cross-sectional area, u is the fluid velocity in the wellbore, $\boldsymbol{e}_t$ is the unit vector in the tangential direction of the wellbore that indicates the flow direction, f_D is the Darcy–Weisbach friction factor, and d_h is the hydraulic diameter. The second term on the right-hand side accounts for the frictional energy loss, Q is the source or sink term, and Q_b is the heat transferred between the fluid and formation through the wellbore wall.

The momentum balance and mass conservation equations are given as:

$$-\nabla_t p \cdot \boldsymbol{e}_t - \frac{1}{2} f_D \frac{\rho_w}{d_h} |u| u + \boldsymbol{F} \cdot \boldsymbol{e}_t = 0 \tag{11}$$

$$\nabla_t \cdot (A \rho_w u \boldsymbol{e}_t) = 0 \tag{12}$$

where $\boldsymbol{F}$ is an external force (e.g., gravitational forces and body forces) per unit volume.

The energy consumed by the pump P_p is given as:

$$P_p = \frac{m_{wf}(h_2 - h_1)}{\eta_p \eta_{pm}} \tag{13}$$

where m_{wf} is the mass flow rate of the working fluid; h_1 and h_2 are the enthalpies of the working fluid before and after pumping, respectively; and η_p and η_{pm} are the isentropic and mechanical efficiencies of the pump, respectively.

The raw output of the turbine P_t is given as:

$$P_t = m_{wf}(h_3 - h_4)\eta_t \eta_{tm} \tag{14}$$

where h_3 and h_4 are the enthalpies of the working fluid before and after passing through the turbine, respectively, and η_t and η_{tm} are the isentropic and mechanical efficiencies of the turbine, respectively.

Based on energy conservation, the mass flow rate of the cooling fluid m_{cf} can be calculated as:

$$m_{cf} = \frac{m_{wf}(h_4 - h_1)}{C_{p,c}(T_6 - T_5)} \tag{15}$$

where $C_{p,c}$ is the specific heat capacity of the cooling fluid and T_6 and T_5 are the cooling fluid temperatures at the outlet and inlet of the condenser, respectively.

Owing to the scarcity of water in Saudi Arabia, air was used as the cooling fluid. Therefore, T_5 equals the ambient temperature.

The installation cost as a function of the electricity generation capacity P is given as (Hackstein and Madlener, 2021):

$$C_{in} = 3000 e^{-0.008(P-1)} \tag{16}$$

Because the installation cost is determined in the design stage of the power plant, the electricity generation capacity refers to the design capacity.

The operation and management (O&M) cost is a function of the electricity generation capacity $P(t)$ (Sanyal, 2005):

$$C_{om} = 0.02e^{-0.0025(P(t)-5)} \quad (17)$$

Therefore, the annual O&M cost can be calculated as:

$$C_{om,a} = 1000\int_0^{8760} C_{om}P(t)\mathrm{d}t \quad (18)$$

The drilling cost of one geothermal well as a function of well length L is given as (Lukawski et al., 2014):

$$C_d = (1.72 \times 10^{-7}L^2 + 2.3 \times 10^{-3}L - 0.62) \times 10^6 \quad (19)$$

Appendix B: Validation of power plant design and off-design models

The design and off-design results of our in-house simulator were compared with the results reported by Gao and Liu (2017). The design conditions are listed in **Table S1**. R134a and water were used as the working fluid and cooling fluid in the validation model, respectively.

Table S1. Design conditions.

Parameters	Unit	Value
Geothermal design temperature	°C	150
Geothermal reinjection temperature	°C	≥70
Geothermal production rate	kg/s	10
Ambient temperature	°C	20
Condenser pinch temperature	°C	5
Pump isentropic efficiency	%	70
Turbine isentropic efficiency	%	80
Cooling water pump head	m	20
Evaporator pinch temperature	°C	10
Superheating degree	°C	5
Subcooling degree	°C	2

The design results are listed in **Table S2**.

Table S2. Design results.

Parameter	Unit	Gao and Liu	In-house simulator	Relative error
Pump pressure	bar	17.87	18.07	1.12%
Condensing pressure	bar	4.01	4.03	0.50%
Turbine inlet temperature	°C	99.4	98.8	0.60%
Net power	kW	330.4	328.7	0.51%
Working fluid mass flow rate	kg/s	8.07	8.05	0.25%

For off-design validation, the results from two scenarios were compared, with variations in the geothermal temperature and production rate. The net power P_{net} values are shown in **Table S3** and **Table S4**.

Table S3. Off-design results at different geothermal temperatures.

Geothermal temperature (°C)	P_{net} reported in Gao and Liu	P_{net} of the in-house simulator	Relative error
135	262.62	259.63	1.14%
140	287.54	283.70	1.34%
145	313.08	308.42	1.49%
155	365.40	358.47	1.90%
160	392.21	385.67	1.67%

Table S4. Off-design results at different geothermal production rates.

Geothermal production rate (kg/s)	P_{net} reported in Gao and Liu	P_{net} of the in-house simulator	Relative error
7	254.52	257.70	1.25%
8	285.36	287.40	0.72%
9	313.95	311.79	0.69%
11	361.36	354.60	1.87%
12	380.44	374.21	1.64%

Appendix C: Supplementary tables

The properties of the overburden formations are given in **Table S5**. The porosity value of the Burqan formation is not given owing to spatial heterogeneity.

Table S5. Properties of the overburden formations.

Formation	Lithology	Thickness (m)	Thermal conductivity (W/m/K)	Specific heat capacity (J/kg/K)	Density (kg/m^3)	Porosity
Ghawwas	Sandstone	1767	1.8	825	2350	0.1
Mansyiah	Evaporite	328	5.0	1050	2400	0.05
Jabal Kirbit	Limestone	191	1.6	850	2500	0.05
Burqan	Sandstone	200	2.0	747.6	2600	/

The properties of the components in the wellbore model are listed in **Table S6**.

Table S6. Properties of wellbore components (Shi et al., 2019).

Component	Diameter or thickness (m)	Thermal conductivity (W/m/K)
Production tubing	0.15	43.5
Inner layer	0.01	43.5
Insulation layer	0.015	0.026
Outer layer	0.01	43.5
Casing	0.01	43.5
Cement	0.03	0.7

The values of the parameters used for calculating the overall heat-transfer coefficient are listed in **Table S7**.

Table S7. Parameters for the overall heat-transfer coefficient (Li et al., 2017; Li et al., 2020).

Parameter	Unit	Value
Inner diameter of tubes d_{i}	m	0.02
Outer diameter of tubes d_{o}	m	0.025
Geothermal water fouling resistance $R_{\mathrm{i,w}}$	m^2·K·W^{-1}	3.4×10^{-4}
Cooling fluid fouling resistance $R_{\mathrm{i,c}}$	m^2·K·W^{-1}	3.5×10^{-4}
Working fluid fouling resistance $R_{\mathrm{o,c}}$	m^2·K·W^{-1}	1.7×10^{-4}
Tube wall thermal conductivity λ_t	W/(m·K)	380
Geothermal water velocity in tubes $v_{\mathrm{i,w}}$	m/s	1
Cooling fluid velocity in tubes $v_{\mathrm{i,c}}$	m/s	15
Working fluid velocity outside tubes in evaporator $v_{\mathrm{o,eva}}$	m/s	1
Working fluid velocity outside tubes in condenser $v_{\mathrm{o,cond}}$	m/s	8

The electricity price for different usage purposes in the Kingdom of Saudi Arabia (KSA) are given in **Table S8**.

Table S8. Electricity prices in the KSA (source: Saudi Electricity Regulation Authority).

Purpose	Price (SAR/kWh)	
	1–6000 kWh	>6000 kWh
Residential	0.18	0.3
Commercial	0.2	0.3
Agricultural	0.16	0.2
Governmental	0.32	
Industrial	0.18	
Private schools & health facilities	0.18	

The optimal solutions in economic optimizations are given in **Table S9**.

Table S9. Optimal results of the economic optimization scenario.

LCOE optimization							
Risk	T_{inj} (°C)	L_w (m)	$T_{g,d}$ (°C)	$q_{g,d}$ (kg/s)	$T_{am,d}$ (°C)	$\epsilon(LCOE)$ (US¢/kWh)	$\sigma(LCOE)$ (US¢/kWh)
Low	84.25	394.58	98.43	47.55	14.13	24.96	0.013
Median	77.14	400.92	122.85	51.50	18.46	21.14	0.28
High	74.70	418.77	125.18	62.22	34.72	14.81	0.49
NPV optimization without the FIT							
Risk	T_{inj} (°C)	L_w (m)	$T_{g,d}$ (°C)	$q_{g,d}$ (kg/s)	$T_{am,d}$ (°C)	$\epsilon(NPV)$ (×10^6 US$)	$\sigma(NPV)$ (×10^6 US$)
Low	90.83	398.61	92.75	47.09	17.70	−10.22	0.0027
Median	87.22	366.80	91.51	51.33	33.02	−8.87	0.074
High	75.18	386.52	95.43	65.66	38.43	−7.92	0.13
NPV optimization with the FIT							
Risk	T_{inj} (°C)	L_w (m)	$T_{g,d}$ (°C)	$q_{g,d}$ (kg/s)	$T_{am,d}$ (°C)	$\epsilon(NPV)$ (×10^6 US$)	$\sigma(NPV)$ (×10^6 US$)
Low	92.02	403.75	95.11	49.24	12.44	0.43	0.0075
Median	74.51	396.19	116.70	55.33	18.50	10.65	0.81
High	74.74	443.87	121.76	62.28	34.54	19.53	1.52

Appendix D: Supplementary figures

The monthly average temperature of NEOM is presented in **Fig. S1**. The period from May to October is categorized as the summer season and that from November to April is categorized as the winter season.

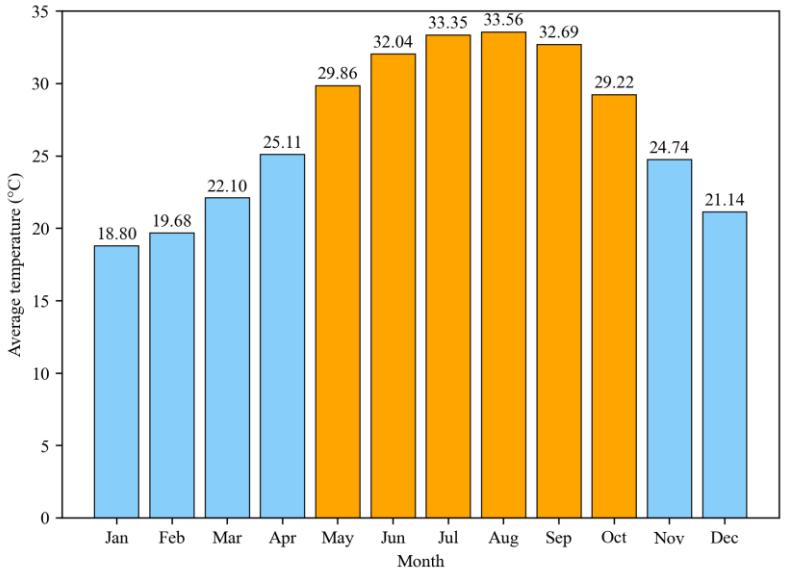

Fig. S1. Monthly average temperature of NEOM (Aljohani et al., 2024).

The permeability and porosity fields of the reservoir discussed in this work were mainly sourced from the work of Al-Laboun et al. (2014). They measured the permeability and porosity of 81 sandstone samples obtained from six outcrops in the Burqan formation in the lab. The permeability and porosity distributions reported in their work are presented herein. Permeability ranged from 36–10502 mD, as shown in **Fig. S2(a)**. The mean value of permeability was approximately 2500 mD. Similarly, porosity ranged from 7%–34%, as shown in **Fig. S2(b)**. There was only one case with 7% porosity, which was considered as an outlier. Therefore, porosity was considered to lie in the range of 15.35%–34.12%, with a mean of ~27%. The permeability and porosity fields of the 2,000 cases were generated based on the aforementioned ranges. Permeability ranged from 20 to 11000 mD, with a mean of approximately 2600 mD, consistent with permeability data reported in the literature. Porosity ranged from 18% to 32%, with a mean of 28.5%, which also aligned with porosity data reported in the literature. As for the other reservoir parameters, such as thermal conductivity, specific heat capacity, and Young's modulus, there were no reported data for the Burqan formation. Therefore, commonly reported ranges for sandstone in the literature, such as Hoteit et al. (2023), were used in this work. The 2,000 simulation cases were sufficient to describe the characteristics of the target formation (Burqan) in NEOM, particularly the permeability and porosity fields.

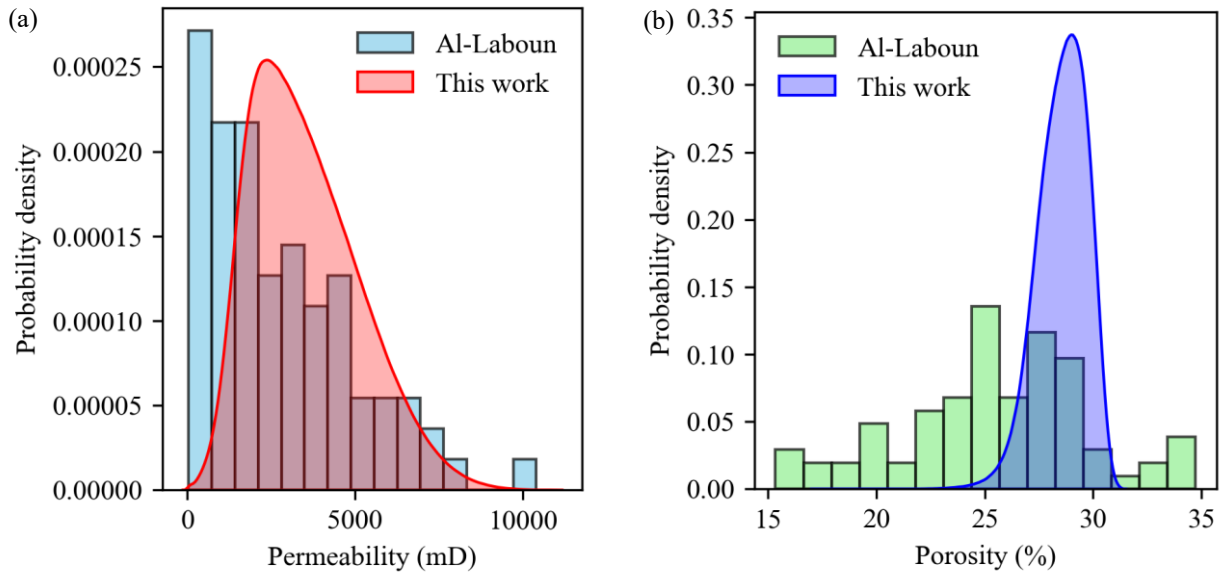

Fig. S2. Justification of the heterogeneous field: distribution of (a) permeability and (b) porosity.

Notably, 50 realizations were generated to account for reservoir uncertainty and predict production temperatures and electricity output using the well-trained surrogate models of the reservoir and power plant, respectively. To demonstrate the accuracy of the surrogate models during multiobjective optimization, the prediction results of the surrogate models were benchmarked with simulation results. The predicted production temperatures of all realizations at all risk levels were first benchmarked with corresponding simulation results predicted by COMSOL Multiphysics. The temperature results at 10^{th} percentile (P10), 50^{th} percentile (P50), and 90^{th} percentile (P90) were highlighted. Then, the prediction results of electricity output were compared with simulation results of the in-house power plant simulator. However, one single simulation performed by our in-house simulator required approximately 6 min on average, which made it highly time consuming to validate all the realizations (3050 simulations) at each risk level. Therefore, only the results of P10, P50, and P90 realizations at each risk level were validated. The benchmark results are shown in **Fig. S3**. The production temperature and electricity output results generally exhibited high consistencies between the surrogate models and corresponding simulators, except for some tolerable deviations at certain timesteps, demonstrating the accuracy of the surrogate models during optimization and the reliability of results.

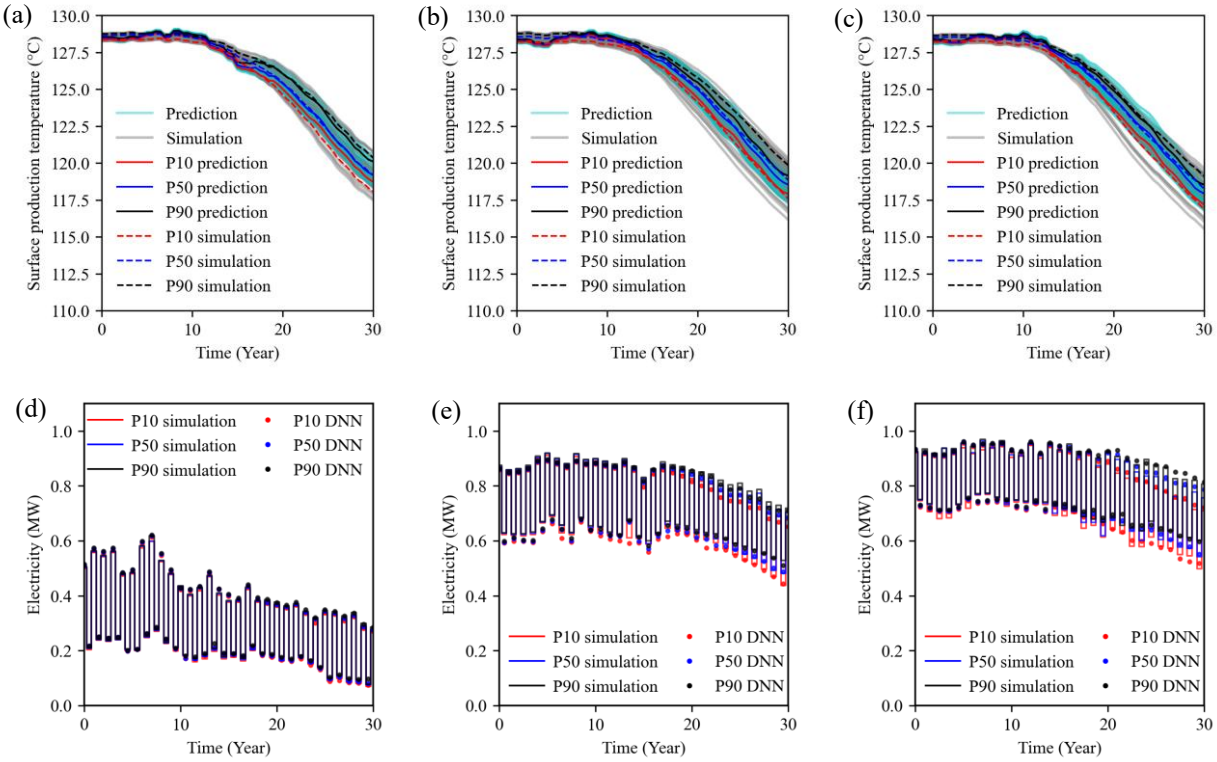

Fig. S3. Benchmarking of surrogate models and simulators: temperature benchmarking at the (a) low risk level, (b) median risk level, (c) and high risk level. Electricity output benchmarking at the (d) low risk level, (e) median risk level, and (f) high risk level.

The temperature and electricity profiles also support our previous analyses. The median- and high-risk solutions showed similar production temperature profiles due to similar operational parameters. The stair-wise fluctuation of electricity output within a year was mainly caused by different ambient temperatures in the summer and winter seasons. The condenser increased the mass flow rate of air to maintain proper condensation in summer owing to a high ambient temperature, which reduced the net electricity output. The low-risk solution had the least electricity generation capacity due to the low design geothermal temperature, geothermal fluid mass flow rate, and ambient temperature. The high-risk solution achieved a higher electricity output than the median-risk solution. However, the high-risk solution has larger differences between the P10, P50, and P90 results at the late stage of the power plant's lifetime (after ~20 years), which indicates a higher risk in delivering the highest electricity output.

References

Al-Laboun, A., Al-Quraishi, A., Zaman, H., et al. Reservoir characterization of the burqan formation sandstone from midyan basin, northwestern saudi arabia. Turkish Journal of Earth Sciences, 2014, 23(2): 204-214.

Aliyu, M. D., Chen, H. Sensitivity analysis of deep geothermal reservoir: Effect of reservoir

parameters on production temperature. Energy, 2017, 129: 101-113.
Aljohani, Z., Asiri, A., Al-Awlaqi, S., et al. Assessment of solar energy availability and its potential applications in neom region. Renewable Energy Research and Applications, 2024, 5(1): 11-19.
Biot, M. A. Theory of elasticity and consolidation for a porous anisotropic solid. Journal of applied physics, 1955, 26(2): 182-185.
Cao, Z., Zhang, G., Liu, Y., et al. Influence of backfilling phase change material on thermal performance of precast high-strength concrete energy pile. Renewable Energy, 2022, 184: 374-390.
Gao, T., Liu, C. Off-design performances of subcritical and supercritical organic rankine cycles in geothermal power systems under an optimal control strategy. Energies, 2017, 10(8): 1185.
Hackstein, F. V., Madlener, R. Sustainable operation of geothermal power plants: Why economics matters. Geothermal Energy, 2021, 9(1): 10.
Hoteit, H., He, X., Yan, B., et al. Uncertainty quantification and optimization method applied to time-continuous geothermal energy extraction. Geothermics, 2023, 110: 102675.
Li, J., Liu, Q., Duan, Y., et al. Performance analysis of organic rankine cycles using r600/r601a mixtures with liquid-separated condensation. Applied Energy, 2017, 190: 376-389.
Li, J., Yang, Z., Hu, S., et al. Effects of shell-and-tube heat exchanger arranged forms on the thermo-economic performance of organic rankine cycle systems using hydrocarbons. Energy Conversion and Management, 2020, 203: 112248.
Lukawski, M. Z., Anderson, B. J., Augustine, C., et al. Cost analysis of oil, gas, and geothermal well drilling. Journal of Petroleum Science and Engineering, 2014, 118: 1-14.
Sanyal, S. K. Cost of geothermal power and factors that affect it. Paper Presented at Proceedings of World Geothermal Congress, 2005.
Shi, Y., Song, X., Wang, G., et al. Study on wellbore fluid flow and heat transfer of a multilateral-well co2 enhanced geothermal system. Applied Energy, 2019, 249: 14-27.